Experimental Thermal and Fluid Science 69 (2015) 99–110

Contents lists available at ScienceDirect

Experimental Thermal and Fluid Science

journal homepage: www.elsevier.com/locate/etfs

Studies of plug formation in microchannel liquid–liquid flows using advanced particle image velocimetry techniques

Maxime Chinaud, Eyangelia-Panagiota Roumpea, Panagiota Angeli *

Department of Chemical Engineering, University College London, Torrington Place, London WC1E 7JE, UK

ARTICLE INFO

Article history:
Received 21 April 2015
Received in revised form 23 July 2015
Accepted 30 July 2015
Available online 4 August 2015

Keywords:
Liquid–liquid
Plug flow
Microchannels
Micro-PIV
Bright field PIV

ABSTRACT

Two complementary micro Particle Image Velocimetry (μPIV) techniques have been developed in this work to study plug formation at a microchannel inlet during the flow of two immiscible liquids. Experiments were conducted for different fluid flow rate combinations in a T-junction, where all branches had internal diameters equal to 200 μm. The dispersed phase was a water/glycerol solution and was injected from the side branch of the junction, while the continuous phase was silicon oil and was injected along the main channel axis. In the two-colour μPIV technique two laser wavelengths are used to illuminate two different tracer particles, one in each fluid, and phase averaged velocity profiles can be obtained in both phases simultaneously. In the high speed bright field μPIV technique, a backlight illuminates the test section, where the dispersed phase plug is seeded with tracer particles. This approach allows velocity profiles of the forming dispersed plugs to be followed in time.

Non-dimensional plug lengths were found to vary linearly with the aqueous to organic phase flow rate ratio, in agreement with a well-known scaling correlation. The flowrate ratio also affected the velocity profiles within the forming plugs. In particular, for a ratio equal to one, a vortex appears at the tip of the plug in the early stages of plug formation. The interface curvature at the rear of the forming plug changes sign at the later stages of plug formation and accelerates the thinning of the meniscus leading to plug breakage. The spatially resolved velocity fields obtained in both phases with the two-colour PIV show that the continuous phase resists the flow of the dispersed phase into the main channel at the rear of the plug meniscus and causes the change in the interface curvature. This change of interface curvature was accompanied by an increase in vorticity inside the dispersed phase during plug formation.

1. Introduction

Flows in small channels, with dimensions less than 1 mm, have been the subject of many investigations recently. At these scales, flows are generally laminar and governed mainly by viscous and interfacial forces, while inertial and gravity forces are small. The thin fluidic films and small fluid volumes improve heat and mass transfer rates which result in more uniform concentration and temperature fields and allow better process control compared to large scale systems; these features can enhance efficiency and reduce waste [5]. Microchannel multiphase flows in particular have found many applications in areas such as chemical analysis and synthesis, pharmaceuticals processing and thermal management systems [3,30]. The increased surface to volume ratio in microchannels favours multiphase processes where interfacial mass or heat transfer are important.

In multiphase microchannel flows, the surface/interfacial forces can affect significantly the flow patterns that form. Understanding the hydrodynamic characteristics of the different flow patterns and their transitions is a key step to properly design small scale multiphase systems. Apart from the operational conditions such as mixture velocity and phase flow rate ratio, flow patterns in small channels depend also on the geometry of the inlet, the wettability of the channel wall and the flow initialization conditions [38,13,32]. Some of the common flow patterns in both gas–liquid and liquid–liquid systems are annular, segmented (slug, plug), and dispersed flow. Segmented flow in particular, tends to appear for a wide range of operational conditions and has been the subject of many investigations [38,6,16,9]. This pattern is characterized by dispersed phase plugs (or in the case of gas–liquid systems, Taylor bubbles) with equivalent diameter larger that the channel diameter, that flow along the channel separated by the continuous phase slugs. In many cases a thin film of the continuous phase separates the plugs from the channel wall, while circulation patterns form within the plugs and the slugs. Both these characteristics enhance

* Corresponding author.
E-mail address: p.angeli@ucl.ac.uk (P. Angeli).

http://dx.doi.org/10.1016/j.expthermflusci.2015.07.022
0894-1777/

mass transfer and make plug flow one of the preferred patterns for mass transfer processes in small scale units.

Liquid–liquid flows in small channels have found applications in the production of emulsions where the controlled conditions lead to very narrow drop size distributions, and in two phase extraction separations and reactions. Experimental studies have shown that the flow pattern map depends not only on the phase flow rate ratio but also on the phase that is injected first in the test section [32]. Kashid et al. [18] investigated the effect of flow rates on the flow pattern map for a Y-shaped junction and found good agreement between experimental velocity profiles within the plugs compared to numerical simulations. Zhao et al. [42] studied the effect of the flow rate ratio on the stability of different flow regimes. Dessimoz et al. [6], who studied liquid–liquid flows in channels using both T and Y-shaped inlet junctions, linked the different flow regimes to the Capillary number. They showed that slug flow formed at high values of surface tension (by adding base in the aqueous phase) while parallel flow was observed when surface tension was decreased (by adding acid in the aqueous phase). Pressure drop during plug flow has also been studied and models have been developed which generally consider two contributions: frictional effects from the two phases and effects from the presence of interfaces [4,17,16,13,38].

In contrast to the relatively large number of investigations on fully developed plug flow, there are few experimental and theoretical studies on plug formation at the channel inlet mainly concerned with the final plug length [9,12,16]. Computational fluid dynamics models have also been developed for plug formation but are not supported by detailed experimental measurements of velocity fields or time evolution of the interface deformation and breakage. A difficulty arises from the high speed of the phenomena and particularly the breakage of the meniscus of the dispersed phase as it emerges from the inlet.

Optical based velocity measurements, particularly Particle Image Velocimetry (PIV), have been successfully applied to microchannel flows. In conventional PIV systems applied to large scale flows [40,26], a pulsed planar laser light illuminates the fluid seeded with tracer particles, and the light reflected from the tracers is captured by a digital camera. The depth of field of the optical lens – camera system is generally larger than the thickness of the light sheet [29] and the plane of measurement is completely defined by the laser sheet. Velocity vectors are calculated from the displacement patterns of the particles, found by cross correlating successive images, and the time delay between the images. The accuracy of the PIV measurements is of the order of 0.1 pixels [35] and is limited by the variation of particle image intensity [26]. In volumetric PIV measurements, the whole flow channel is illuminated and the depth of field is less than the thickness of the light sheet. This is the configuration used in microfluidic applications and has led to the development of the micro-PIV (μPIV) approaches [33,36,14,31]. To overcome the reflections of the surrounding channel walls and enhance the signal of the rather small particles used in microchannels (a few microns or less), fluorescent particles are commonly used [23,1]. Images are collected from the camera either via a microscope or microscope lenses which provide magnification of usually two orders of magnitude.

Liquid–liquid plug flow in microchannels has already been investigated with μPIV by a number of researchers for a variety of fluids [15,34,21,8,39]. These studies have mainly focused on the plug propagation in the main channel and the recirculation patterns in the plug and slug phases. However, studies on the aqueous/organic phase plug flow formation at the channel inlet are limited [9,22].

In two-phase μPIV applications usually one of the phases is seeded with tracers and velocity profiles are obtained in that phase only. There have been limited attempts to visualize both phases simultaneously that resulted in the two-colour systems. In this approach, two different laser wavelengths are generated and each one excites one of two different tracers seeded in each of the two phases respectively [27,2,28]. Each phase is usually visualized by a separate camera, while additional optical components such as dichroic mirrors, optical filters or beam splitters increase the complexity of the measuring system. An additional difficulty comes from the unavailability in general of tracers that can be suspended in organic phases (the second phase in the majority of liquid–liquid applications), as most commercial particles have been developed for aqueous systems. Oishi et al. [27] used a confocal two-colour μPIV system to visualize liquid–liquid plug formation in a T-shaped junction. The commercial particles used in the organic phase were dried from aqueous commercial solutions. The cameras commonly used in two-colour μPIV systems are low frequency; this seems necessary as usually one of the tracers has low intensity which requires the use of sensitive low speed cameras. Plug formation and meniscus breakage at the channel inlet, however, are very fast and high speed visualization systems (above 1 kHz) are then required to adequately resolve the phenomena in time.

So far, very little attention has been given to bright field PIV (shadowgraphy) velocity measurements for microfluidic applications [11]. In this technique, tracer particles are illuminated by a white backlight and their shadow is recorded, instead of fluorescence. This method, based on the BW contrast measurements between the particles shadow and the optical background, is less complex than conventional μPIV as it does not require laser lights coupled with suitable fluorescent particles, while it can be combined with high speed cameras for high frequency image acquisition. Tsaoulidis [39] used an image acquisition system based on bright field PIV principles to visualize the recirculation patterns in fully formed liquid plugs in small channels. The technique has not been applied before to visualize the high speed plug formation in the inlet zone of a microchannel.

The main aim of this paper is to present the application of two innovative velocity measurement approaches, two-colour μPIV and high speed bright field PIV to the study of liquid–liquid plug formation in microchannels. In what follows, the development of the two velocity measurement techniques is first presented and the experimental system is described. Results on plug formation are then shown and discussed. Particular attention has been given to the image analysis and data treatment procedure.

2. Experimental setup

Plug formation in liquid–liquid flows was investigated in a circular microchannel (Dolomite) with 200 μm internal diameter (ID). The fluid mixing zone is a T-junction with side branches equal to 200 μm ID (Fig. 1). The microchannel is made of two semi-circular grooves etched in two different quartz chips that have been thermally bonded together. Each fluid is driven independently by a syringe pump (KDS Scientific®). Experiments were carried out for fluid flowrates ranging from 0.3 to 0.9 mL/hr. The organic phase used in this work is silicon oil with 155 mPa s viscosity and 1070 kg m^{-3} density. The aqueous phase is an aqueous-glycerol mixture (55% w/w) with 7 mPa s viscosity and

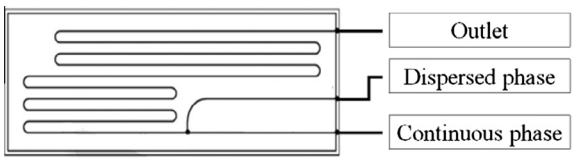

Fig. 1. Top view of the test section.

1142 kg m^{-3} density. The aqueous phase is injected from the top branch of the T-junction. For all condition studied, an aqueous plug formed in the T-junction while the more viscous oil was always the continuous phase. Experiments were performed for different values of the mixture velocity, U_{mix}, and the flowrate ratio, r, defined as follows:

$$U_{mix} = (Q_c + Q_d)/A,$$

$$r = Q_d/Q_c,$$

where A denotes the cross section of the channel and $Q_{d/c}$ represents respectively the flow rate of the dispersed (aqueous) or the continuous (organic) phase. The different experimental conditions are summarized in Table 1 with the corresponding Capillary numbers, calculated as $Ca = \mu_c U_{mix}/\sigma$ where μ_c is the continuous phase viscosity and σ is the interfacial tension between the two liquids, which is equal to σ = 33 mN m^{-1}.

2.1. Two-colour μPIV technique

The two-colour μPIV technique is based on the use of two laser wavelengths to illuminate two different particle types, each seeded in one of the phases of a two-phase mixture. In contrast to the few reported applications in the literature, where two lasers have been used to generate the two distinct wavelengths [28], in this work the same laser was used to generate simultaneously both wavelengths. The laser is a dual beam (with two independent laser cavities) Nd-YAG unit (Nano PIV series, Litron Laser). The initial beam has a wavelength in IR (1066 nm). Using heated crystals, two different wavelengths, a blue (355 nm) and a green (532 nm) are then generated by each laser cavity. The time delay between the two cavities is controlled by a synchronization unit (TSI synchronizer). Both laser beams are guided through an optical fibre to the microscope unit (Nikon Ti-400), and are reflected by a dichroic mirror on to the microscope objective where the test section is placed (see Fig. 2a).

One of the difficulties in the application of two-colour μPIV is the identification of appropriate tracer particles that absorb and emit at the required wavelengths and can be suspended in aqueous and organic phases. Although there are many options for particles that can be used in aqueous phases, there are very few particles commercially available that can be suspended in organic phases. For the aqueous phase, red fluorescein coated polystyrene particles with mean diameter 1 μm (Thermo Scientific; Flouro max Fluorescent Red (542 nm/612 nm)) were used. The particles added in the organic phase were blue fluorescein coated polystyrene particles with mean diameter 1 μm (Thermo Scientific; Flouro max Fluorescent Blue (365 nm/447 nm)). When purchased, the blue particles were suspended in an aqueous solution and had to be dried in a vacuum dehydrator at 25 °C. They were then suspended in the oil phase within an ultrasound bath to break any clusters.

The microscope dichroic mirror is designed to pass the 440 ± 40 nm and the 610 ± 40 nm wavelengths reflected from the particles. Consequently, the incoming wavelengths from the laser are reflected while the emitted signals by the particles pass through the mirror. The fluorescent signals emitted from the particles are then directed through the objective and the dichroic mirror into a beam splitter unit (Tucam, Nikon). Within the beam splitter unit, the fluorescent light from the particles is brought into a second dichroic mirror which reflects the 410 ± 40 nm and passes the 610 ± 40 nm wavelengths. The blue signal is directed to a high sensitivity camera (Sensicam, PCO), while the red wavelength is directed to a CCD camera (TSI Powerview 4MP). In this particular system, two different cameras have been used to see the two different phases. When a single camera is used, beam energy losses are reduced but the discrimination between the two phases is more difficult. With two cameras the phase discrimination is easier but additional barrier filters need to be installed in front of each camera which increase energy losses. For the blue signal the barrier optical filter is a pass band filter centred at 450 ± 50 nm, while for the red signal a high pass filter with a cut wavelength around 650 nm is used.

Table 1
Summary of experimental conditions.

Case	Q_c (mL h^{-1})	Q_d (mL h^{-1})	U_{mix} (m s^{-1})	r	Ca
1	0.3	0.3	0.0053	1	0.0259
2	0.3	0.6	0.008	2	0.0376
3	0.3	0.9	0.0106	3	0.0498
4	0.6	0.3	0.008	0.5	0.0376
5	0.6	0.6	0.0106	1	0.0498
6	0.6	0.9	0.0133	1.5	0.0625

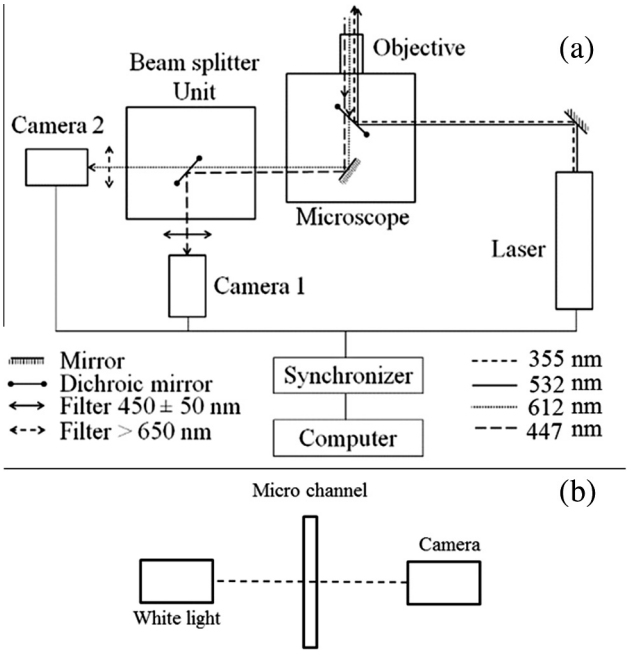

Fig. 2. (a) Schematic of the two-colour PIV system set up. (b) Schematic of the high speed bright field PIV system set up.

The use of the sensitive camera for the blue light is an important feature of this configuration since this fluorescent signal is weak. There is significant energy loss of the initial laser beam in the generation of harmonics and the blue laser beam is the weakest one (approximatively 50% of the initial beam energy). In addition, the multiplication of the dichroic mirror is also decreasing the beam energy. Further energy losses occur at the optical filters. The possibility to increase the gain of the sensitive camera makes this component crucial to record the blue particles signal. An additional complexity when using two cameras is that each has a different sensor, 1270 × 512 pixels for the blue camera and 1024 × 1024 pixels for the red CCD camera. Post- processing is then necessary to match the signal recorded by the two cameras. A raw image of the microchannel unit illuminated with white light is acquired and used as calibration target for both cameras. In the current configuration, the microscope objective has a 10× magnification and each camera has an additional 2× magnification lens. The final resolution is 0.5 μm/pixel for the blue camera and 0.33 μm/pixel for the red camera. The time delay between the two laser cavities as well as the acquisition of the cameras are controlled by a synchronizer unit (TSI instrument); the acquisition rate is 7.25 Hz per image pair. With these specifications the velocities than can be

measured with the red camera range from 0.5×10^{-3} to 0.5 m/s while for the blue camera they range from 0.3×10^{-3} to 0.3 m/s.

2.2. High speed bright field (shadowgraphy) μPIV technique

In the high speed bright field μPIV technique, the flow channel is illuminated with a white light from the back and the shadows of the tracers seeded in a given phase are recorded by BW contrast imaging over successive frames [11]. In the current work, the technique was coupled with a high speed camera which allowed time resolved velocity measurements and was able to capture the interface breakage during plug formation at the channel inlet (see Fig. 2b). The high speed camera (Photron 3000, 1024 × 1024 pixel) had an acquisition frequency of 3 kHz and was equipped with an optical train (TSI instruments) and a long focal distance microscope lens. This configuration provided 40× magnification and a 0.69 μm/pixel spatial resolution. The focal plane was approximatively placed in the centre of the channel along the transverse axis. From the specifications of the microscope lens (NA = 0.42, $n = 1$), the computed depth of field was close to 3 μm [7]. The test section was uniformly illuminated with white light, generated from LED with adjustable intensity. The tracers were 1 μm polystyrene spherical beads coated with red fluorescein (Thermo Scientific; Flouro max Fluorescent Red (542 nm/612 nm)).To improve the quality of the data and enhance the contrast signal, only the water phase was seeded. In addition, complementary measurements of plug length were carried out by recording the flow downstream the inlet. With this configuration velocities ranging from 2×10^{-3} to 0.033 m/s could be measured.

3. Data treatment procedure

3.1. Two-colour μPIV data treatment

For both PIV approaches data is collected in a computer and the velocity fields are treated by using a commercial code (Insight 4G, TSI), as discussed below. One major issue in PIV studies involving two phases is the discrimination and tracing of the interface. Mohamed-Kassim and Longmire [24] in droplet coalescence studies used a small amount of fluorescein to dye the aqueous phase. By increasing the contrast of one phase compared to the other, the interface can then be reconstructed. This process is generally necessary when the refractive index of the test fluids has been matched. When the refractive index is not matched then the interface appears as a bright line. A number of studies have looked at image processing procedures to minimize the interface effect on the computation of the near interface velocity fields (e.g. [37]).

Images taken with the two-colour μPIV system do not show any interface. The optical filters used absorb the wavelengths emitted from the laser that can reflect on the interface, and allow only the wavelengths emitted from the particles to reach the cameras. A snapshot of the images recorded by the two cameras can be seen in Fig. 3 for equal water and oil flow rates of 0.3 mL h^{-1}. No interface can be seen, while it is also clear that the two cameras have different spatial resolution. Interface reconstruction in two-phase systems from μPIV images has been discussed by Yamaguchi et al. [41]. Generally the interface is reconstructed based on the presence of particles in one region. In this study, a procedure (and MATLAB code) has been developed to trace the interface based on particle signal. In the first step the raw image is filtered by using a median filter based on 7 × 7 pixels computation and binarised. Then, the white pixels are dilated using a 7 pixel square shape. Finally, the contour of the white region is fitted giving the reconstructed interface contour. To match the velocity fields of the two phases in the same frame, the contour of the reconstructed interface is used as an adaptive mask that discriminates the phases in each camera.

To improve the velocity field computation, each image was pre-treated by normalizing it with its minimum intensity. The image renormalization appears to be a key step for improving the computation of the vectors from the cross correlation of the images. There is usually a difference in the mean intensity between two consecutive images.

For both cameras, the PIV correlation box size was set to 64 × 64 pixels with 50% spatial overlapping. The different fields of view of the two cameras result in a velocity vector resolution of 10.56 × 10.56 μm for the aqueous phase and of 24 × 24 μm for the organic phase. For the computation of the velocity fields, a recursive Nyquist grid with an FFT correlation calculation was used. The correlation peak position was found with a Gaussian peak algorithm detection. For both phases a velocity range filter was defined and valid velocity vectors were chosen based on standard deviation and primary to secondary peak ratio. The removed false vectors were replaced by the median value computed from the neighbour velocity values using an Insight 4G post-treatment procedure. In each velocity field, vectors outside the corresponding seeded phase were set to zero.

In this particular setup the two-colour μPIV system has been configured with a low frequency acquisition (7.25 Hz per image pair) but with an adjustable time delay between the two laser

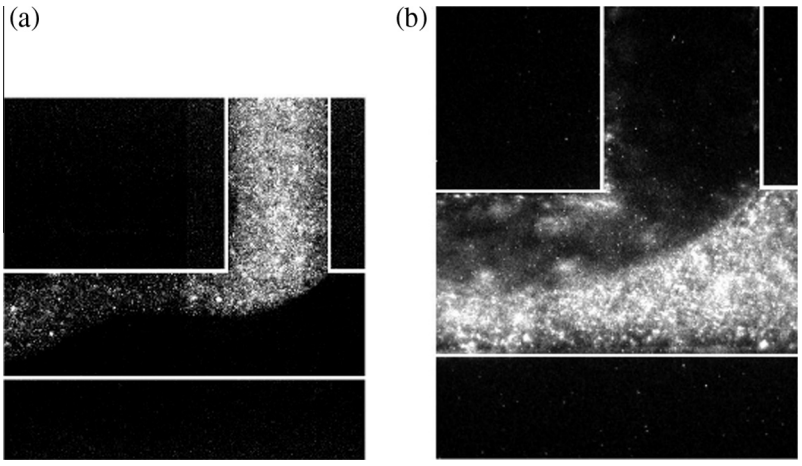

Fig. 3. Images obtained by the two cameras of the two-colour μPIV system of (a) aqueous phase; (b) organic phase. Flow rates of both the organic and the aqueous phase are 0.3 mL h^{-1}.

cavities from 1 μs to 1000 μs. By keeping the spatial resolution constant, the time delay for each experiment was decided so that the maximum particle displacement would not exceed half of the final correlation box size. Because of the low frequency acquisition, image pairs are captured at different stages of the plug formation that are not correlated. For this reason, the data extracted from the two-colour μPIV technique needs to be phase averaged. In order to have time resolved velocity fields measurements, a high speed acquisition system is required.

3.2. High speed bright field μPIV data treatment

The images obtained from the bright field μPIV measurements required different treatment. The technique is based on the BW contrast between the dark particles and the illuminated surroundings. As there are no filters installed, the interface can be seen because there is a slight mismatch of the refractive indices of the two liquid phases. The image pre-treatment procedure is thus simpler than in the case of the two-colour PIV. As can be seen in Fig. 4a for aqueous and organic flow rates equal to 0.3 mL h^{-1} each, the interface appears as a clear black line. As a first step, the grayscale values are inversed. This is necessary because the raw images display the shadow of particles on a white background while PIV image processing codes need bright tracer signals on black background [11]. To facilitate the correlation computation, the optical background of the inverse greyscale image is then removed. The image of the aqueous plug forming in the channel inlet can be seen in Fig. 4b after grey scale inversion and removal of the optical background.

The PIV resolution for bright field μPIV measurements was setup to 32 × 32 pixels with 50% spatial overlapping, which corresponds to 11.04 × 11.04 μm per velocity vector. Similar to the two-colour PIV, the computation of the velocity vectors was based on a recursive Nyquist grid with an FFT correlation calculation. The correlation peak position was computed with Gaussian peak algorithm detection and the validation of the velocity vectors was based on standard deviation and primary to secondary peak ratio. Removed false vectors were replaced with the median value of neighbouring velocity vectors. It should be noted that the raw images of the bright field μPIV technique are better compared to those of the two-colour PIV. In bright field μPIV the data post-treatment involves mainly removal of the false vectors in the organic phase.

The use of a high speed camera means that the different stages of plug formation can be tracked in time, in contrast to the two-colour PIV approach which has low acquisition frequency between image pairs. However, the time delay between two successive high speed images is constant and rather large (equal to 333 ms). When high velocities are present then this time delay in the high speed camera cannot be adjusted to accommodate the large particle displacements and may not be enough to resolve the velocity vectors. This is not a problem in the two-colour PIV system where the time delay between laser pulses is adjustable and can be as small as 1 μs.

4. Results and discussion

Plug formation frequencies and plug lengths were measured with the high speed image acquisition system. A simple scaling law for the length of plugs generated in T-junctions has been developed by Garstecki et al. [9]:

$$\frac{L}{d} = 1 + \alpha \frac{Q_d}{Q_c} \tag{1}$$

where L and d are respectively the plug length and the internal diameter of the channel and α is a constant of the order of one which depends on the geometric characteristics of the T-junction. The equation is compared against the current experimental data obtained at Capillary numbers of the order of 10^{-2} (see Fig. 5). As can be seen the scaling law agrees well with the experimental results for values of α equal to 1.1 ± 0.1.

The plug length multiplied by the plug frequency is plotted against the mixture velocity in Fig. 6. As can be seen, at the low organic (continuous) phase flow rate, the mixture velocity can be approximated by $L * f$ (where f represents the plug formation frequency). At the higher organic phase flow rate, $L * f$ is higher than the corresponding mixture velocity.

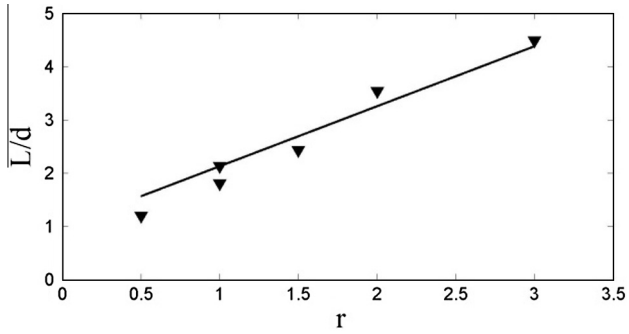

Fig. 5. Normalized plug length versus aqueous to organic phase flow rate ratio. Experimental data are shown as points and Eq (1) as a solid line for $\alpha = 1 \pm 0.1$..

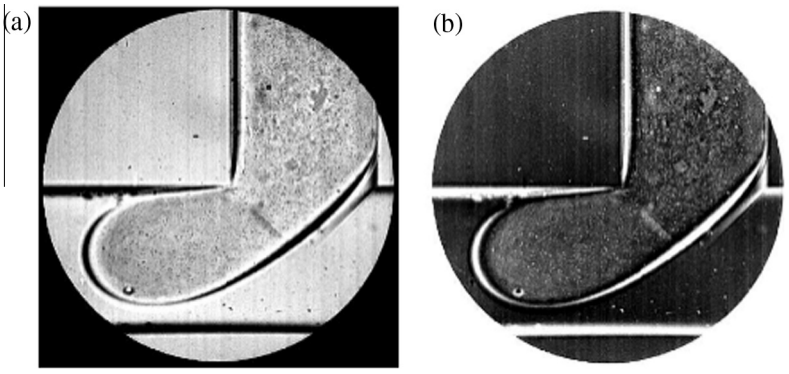

Fig. 4. Images acquired with the bright field μPIV technique. (a) Raw image with tracers in the aqueous phase. (b) Pre-treated image after grey scale inversion and removal of the optical background. Flow rates of both the organic and the aqueous phase are 0.3 mL h^{-1}.

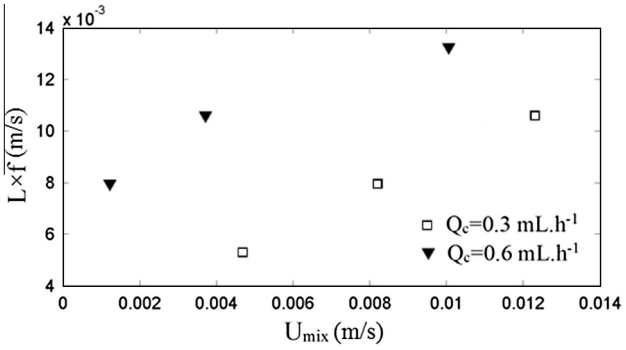

Fig. 6. Plug length multiplied by the plug formation frequency versus the corresponding mixture velocity.

4.1. Plug detachment

The modelling of plug formation in microfluidic junctions has been the subject of a few studies, mainly focusing on channels with rectangular cross section [9,22]. A few visual observations are also available of the plug formation process in T-shaped junctions during liquid–liquid flow in microchannels [10,19]. For convenience the two dimensional problem is considered here (Fig. 7) where the non-dimensional axes are normalized by the width of the main channel as follows, $x^* = x/d$ and $y^* = y/d$. In this configuration the two main radii of the interface curvature are located at the tip and at the rear of the plug. The rear region is generally approximated by a circle in numerical studies [22]. This was found to be correct in this study up to a critical point in plug formation.

The evolution of the plug formation was followed with the high speed bright field μPIV measurements which made possible the precise location of the plug pinch-off point along the microchannel. The dynamics of an aqueous phase plug breakage are shown in Fig. 8 for equal organic and aqueous phase flow rates of 0.3 mL h^{-1}. The time delay between each photograph is 11.3 ms (34 frames). All other investigated flow rates were found to have a similar plug formation process.

In agreement with previous studies [25,20], the observations showed that the pinch-off point is not located at the corner of the T-junction but along the horizontal axis on the top of the channel. In Fig. 8a the previous aqueous plug has just detached. A very thin film remains on the wall which will eventually give a small droplet. The tip of the next aqueous plug is moving into the main channel following the flow direction (Fig. 8b). The plug then grows into the main channel and the radius of curvature of the tip increases (Fig. 8c–e). For the chosen optics and magnification, the tip of the plug leaves the camera field of view before the meniscus breakage. While the plug grows, the distance between the left hand side corner of the T-junction and the interface decreases. At the same time, the radius of curvature at the rear of the plug increases to reach a semi-flat configuration. At constant flow rate this reduction in the flow area of the dispersed aqueous phase will increase the velocity at this point. Interestingly, the reduction in flow area at the corner of the T-junction is followed by a change in the curvature sign of the interface (Fig. 8f and g). The increase in the aqueous phase velocity would be accompanied by a decrease in the local pressure which may in turn change the pressure balance across the interface and induce the change in curvature. This inversion of the curvature of the interface increases the thinning rate of the meniscus and leads to the plug pinch-off (Fig. 8h). The inversion in the curvature in the early stages of the breakage has been noted in the literature previously [22]. It has also been reported that the distance of the plug pinch-off point from the T-junction depends on the input parameters. In this work, the maximum distance along the x-axis is reached for the maximum flow rate ratio ($r = 3$) and is approximately equal to 200 μm. For lower ratios the distance is about 80 μm. Because of the formation of a single satellite droplet during the interface breakage, a very accurate estimate of the position of the pinch-off point is difficult.

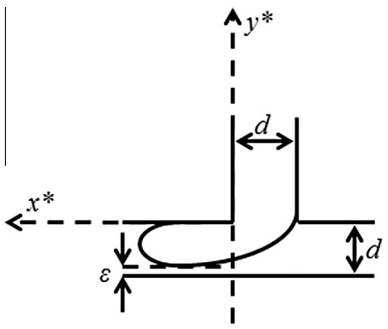

Fig. 7. Schematic of plug formation. The distances d and ε represent respectively the capillary diameter and the thickness of the continuous phase film surrounding the plug.

4.2. Time resolved velocity field measurements

The plug formation process is generally described by considering the balance among three different forces: the surface tension force, the shear stress force and the resistance force on the plug tip as it enters into the main channel. The surface tension and resistance forces tend to stabilize the droplet while the shear stress along the main channel, generated by the flowing continuous phase, tends to distort the interface. The evaluation of the forces is important for describing the different regimes in the plug formation process. The surface tension force can be evaluated from the local radii of the interface curvature using the Laplace law. The principal radius of curvature located at the tip and in the rear of the plug can be approximated by the geometrical parameters of the channel and scaling laws have been proposed in the literature (e.g. Garstecki et al. [9]). The estimates of the various forces, however, have not been linked to the hydrodynamic patterns of the dispersed phase. For the flow rate combinations studied, the instantaneous velocity fields obtained with the high speed bright field μPIV technique are plotted in Figs. 9 and 10. As mentioned previously, very high velocity measurements cannot be acquired with this technique. From the different stages described in Fig. 8, the highest dispersed phase velocities are expected when the thickness of the meniscus decreases after the inversion of the local interface curvature. In this particular stage, the computation of the velocity field was not possible because the displacement of the tracer particles between two successive frames is too large. Two different stages have been chosen to illustrate the velocity fields in the dispersed phase. The first stage (Fig. 9) is at the beginning of the plug formation process, a few frames after the previous plug detachment. In the second stage the rear of the plug has adopted a semi-flat configuration (Fig. 10). In Fig. 9b, c, and f the plug has already entered the main channel. The streamlines start from the top branch of the T-junction towards the direction of the continuous phase flow. In these cases the dispersed phase has higher flowrate than the continuous phase and the plug enters the main channel with reduced hydrodynamic resistance. Just after the meniscus breakage, the new plug is more or less formed in the main channel and the shape of the streamlines is not modified significantly until the inversion of the curvature of the rear of the plug (beginning of the meniscus breakage process). This can be seen in Fig. 10b, c and f where the plug has grown, but the streamlines show a similar motion. The early stage of plug formation for equal

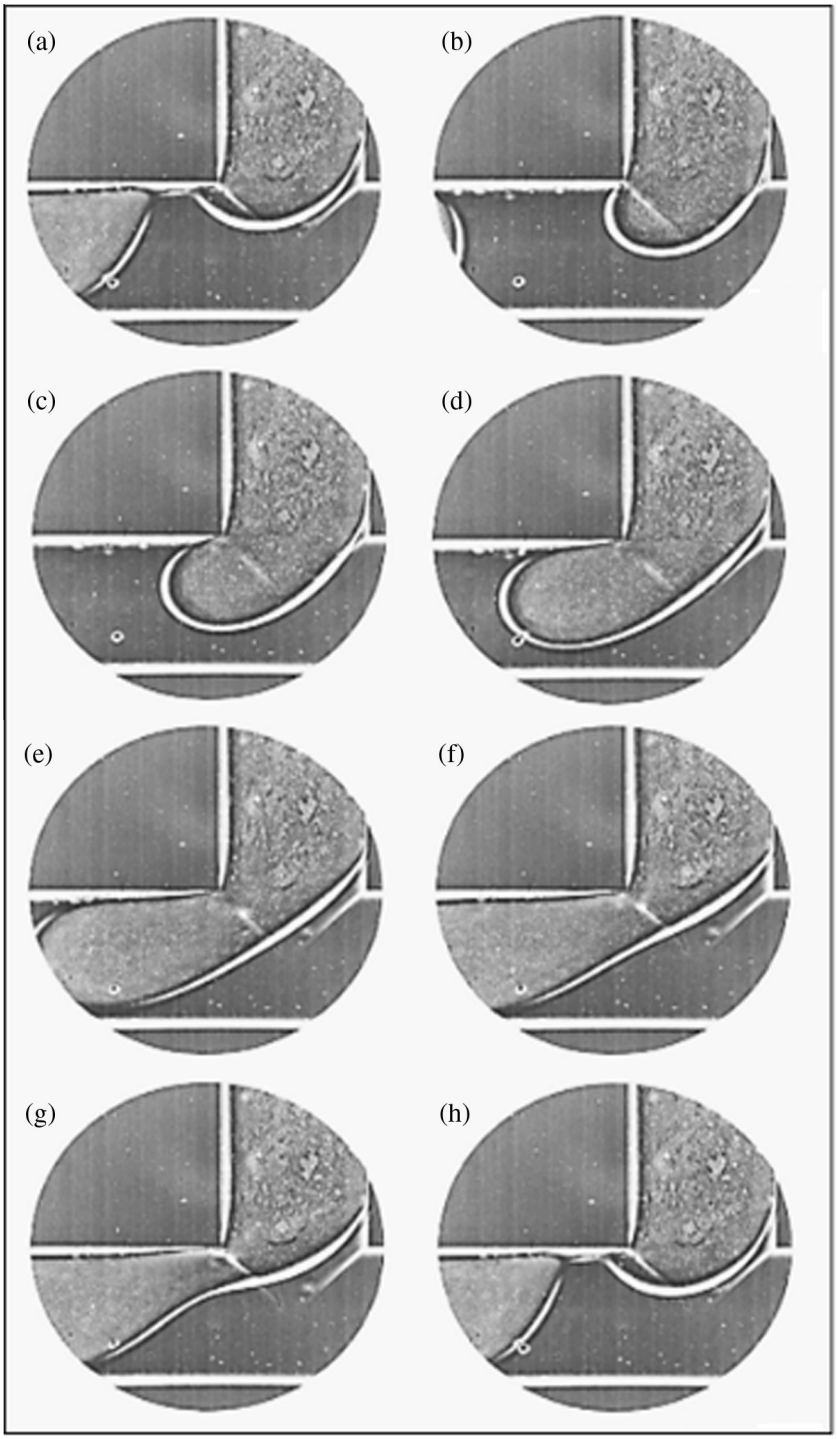

Fig. 8. Meniscus breakage during plug formation for both organic and aqueous phase flow rates of 0.3 mL h^{-1}. The time between images is 11.3 ms. Images (f) and (g) illustrate the change of interface curvature before the meniscus breakage.

flowrates of the two phases can be seen in Fig. 9a and e. In this case the plug is still developing along the vertical axis, with the tip slightly shifted to the direction of the continuous phase flow. This asymmetry generates a change in the horizontal velocity component at position $y^* = 0$, which becomes negative inducing a slight distortion in the streamlines. At the later stage (Fig. 10a and e) the vertical velocity component at $y^* = 0$ becomes positive (direction of the organic phase flow), and the streamlines follow the same pattern as in the cases of higher flow rate ratios. The results for dispersed phase flow rate less than the continuous one (Fig. 9d), show the most interesting hydrodynamic pattern. In this case, the faster continuous phase generates a vortex inside the dispersed phase in the region of the plug tip. The vortex has clockwise motion following the direction of the continuous phase flow. This vortex is then pushed inside the main channel and disappears as the curvature of the rear of the plug increases. At the later stage shown in Fig. 10d the streamlines adopt a similar pattern to the other flow rate ratios. The formation of the vortices at the tip is attributed to the quick retraction of the interface after the breakage. It is suggested that a vortex forms in all cases but decreases

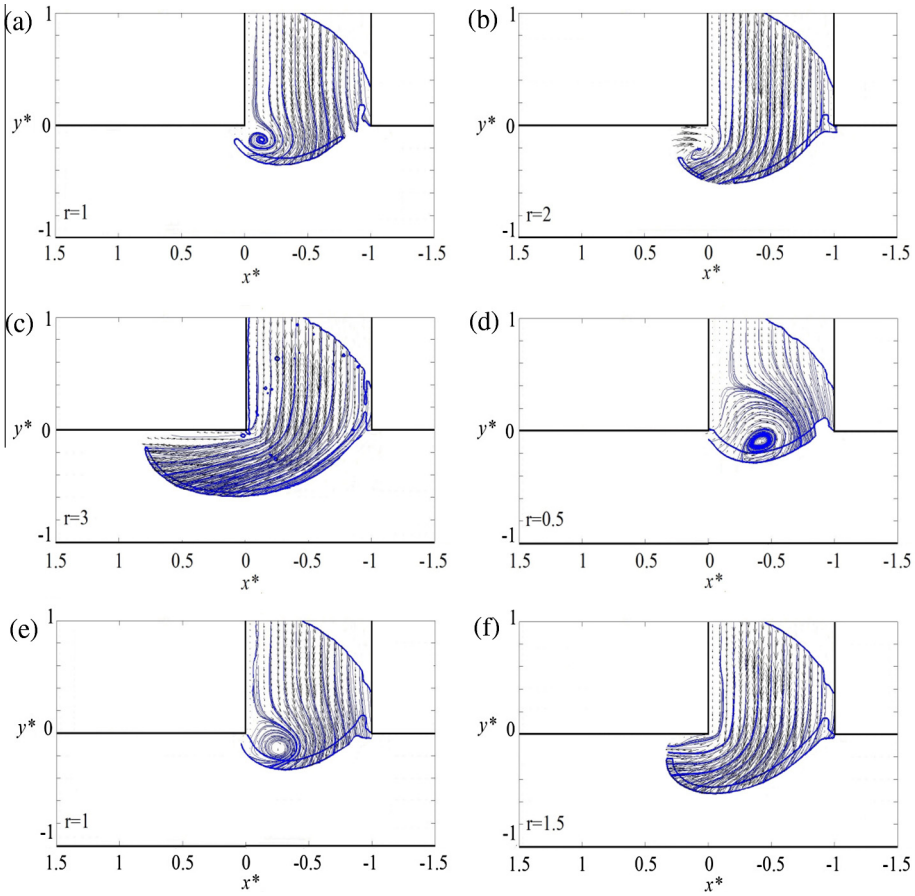

Fig. 9. Instantaneous dispersed phase velocity fields and streamlines in the non-dimensional frame. High speed camera sampling frequency is 3 kHz. The different figures show the following flow rate combinations: (a) 0.3 mL h^{-1} (organic phase) 0.3 mL h^{-1} (aqueous phase), (b) 0.3 mL h^{-1} (organic phase) 0.6 mL h^{-1} (aqueous phase), (c) 0.3 mL h^{-1} (organic phase) 0.9 mL h^{-1} (aqueous phase), (d) 0.6 mL h^{-1} (organic phase) 0.3 mL h^{-1} (aqueous phase), (e) 0.6 mL h^{-1} (organic phase) 0.6 mL h^{-1} (aqueous phase) and (f) 0.6 mL h^{-1} (organic phase) 0.9 mL h^{-1} (aqueous phase). For clarity, the channel boundaries have been added.

when the flow rate ratio increases. For flow rate ratio above 1 (Fig. 9b, c, and f) it is difficult to visualise properly this pattern. For flow rate ratio $r = 0.5$, the vortex remains for a long time on the tip of the plug and corresponds to the highest vortex size measured.

The variations over time of the horizontal velocity components are compared in Fig. 11 for all cases studied. Velocities are compared for (x^*, y^*) equal to $(-0.5, 0)$ (middle of dispersed phase branch where it joins the main channel) because at this position seeded phase was present in all cases and velocities could be computed. The results for water to oil flow rate ratios $r = 0.5$ (solid line) and $r = 2$ (dashed line) are shown in Fig. 11a. At flow rate ratio below 1 a vortex is forming at the tip of the plug (Fig. 9d). At the selected point, the velocity remains negative due to the clockwise motion of the vortex. As the plug grows, the horizontal velocity component increases until it becomes positive. This change in sign indicates that the plug is now within the main channel. The curvature of the rear of the plug increases until it becomes almost flat and the flow inside the dispersed phase follows the direction of the continuous phase flow. At some point, the horizontal velocity component reaches a maximum value before it suddenly decreases when the plug has detached. The velocity becomes then negative again and a new vortex is formed. On the contrary, for flow rate ratio $r = 2$, the horizontal velocity component fluctuates but remains positive. For flow rate ratio above 1, the plug has already entered the main channel from the early stages of formation, and the velocity always follows the direction of the continuous phase flow. In this regime, the increase in velocity corresponds to the diminishing width of the dispersed phase meniscus. The change in the curvature at the rear of the plug leads to an acceleration of the fluid. For flow rate ratio above unity the peaks in velocity are less pronounced. This is attributed to the location chosen for the velocity plots which is far from the pinch off point compared to the other flowrate ratios. The evolution of the horizontal velocity component for equal flowrates of the two phases is shown in Fig. 11b. The plug breakage frequency again matches the peaks in velocity over time. At the initial stages of plug formation the horizontal velocity component is negative. It then increases and becomes positive before it suddenly decreases again to negative values when the plug breaks off.

4.3. Phase averaging velocity field measurements

As discussed before, the time separation between the high speed images in the bright field PIV is not short enough (333 ms in this study) to capture the fast velocities that occur during the thinning of the plug meniscus. This is possible with the two-colour PIV system which uses a straddling camera that allows very short time separation between image pairs. The frequency though of this camera is small (7.25 Hz in this study) and the different plug formation stages cannot be followed in time.

The two-colour PIV velocity profiles are averaged in each phase for different locations of the plug, determined by the position of the plug tip inside the main channel. The tip location was determined with an error of ±50 pixels (±16.5 μm). It was found that good velocity fields were obtained in both phases when about 50

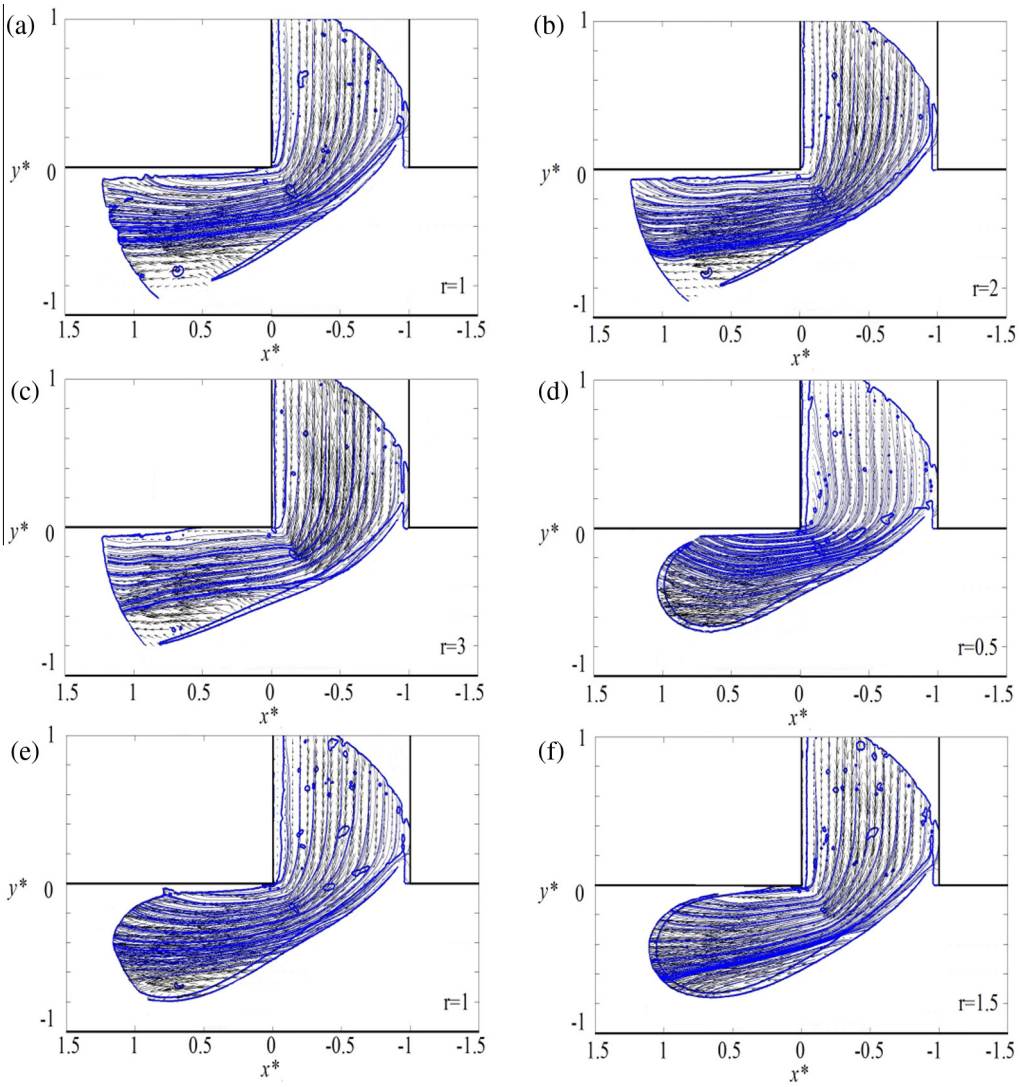

Fig. 10. Instantaneous dispersed phase velocity fields and streamlines in the non-dimensional frame. High speed camera sampling frequency is 3 kHz. The different figures show the following flow rate combinations: (a) 0.3 mL h^{-1} (organic phase) 0.3 mL h^{-1} (aqueous phase), (b) 0.3 mL h^{-1} (organic phase) 0.6 mL h^{-1} (aqueous phase), (c) 0.3 mL h^{-1} (organic phase) 0.9 mL h^{-1} (aqueous phase), (d) 0.6 mL h^{-1} (organic phase) 0.3 mL h^{-1} (aqueous phase), (e) 0.6 mL h^{-1} (organic phase) 0.6 mL h^{-1} (aqueous phase) and (f) 0.6 mL h^{-1} (organic phase) 0.9 mL h^{-1} (aqueous phase). For clarity, the channel boundaries have been added.

images were averaged. The results for a flow rate combination of $Q_c = 0.6$ mL h^{-1} and $Q_d = 0.3$ mL h^{-1} ($r = 0.5$) are discussed here, where bright field PIV showed that a large vortex forms near the tip of the plug early in the plug formation process. The vorticity field in the aqueous phase and the velocity fields in both phases are shown respectively in Fig. 12 for positions of the plug tip in the main channel of approximately (a) 0.75, (b) 1, (c) 1.25 and (d) 1.5 and in Fig. 13 for positions of the plug tip in the main channel of approximately (a) 0.5, (b) 0.75, (c) 1 and (d) 1.25. These different stages can be considered as a chronological sequence of phase averaged fields, although the time between the sequences is not known. The averaged interface has also been added in Fig. 13. The interface shape is not as accurate as the one obtained by high speed bright field μPIV because it is averaged over many images. In the continuous phase velocity field, the three vector lines closest to the channel wall have been removed (Fig. 13) because results there were very noisy even after the averaging.

The vortex at the tip of the plug can be seen in Fig. 12a and b. In the third stage, a counter rotating vortex appears at the rear of the plug which increases in magnitude as the plug proceeds along the channel. The velocity fields show that in the dispersed phase the horizontal velocity component is more pronounced (Fig. 13a). There are however, vertical velocity components at the tip of the plug at the early stages of plug formation and at the rear of the plug. This latter component seems to increase as the plug propagates in the main channel (Fig 13b).

The horizontal and vertical velocity profiles in both phases for the first stage of plug formation (Fig. 13a) are shown in Fig. 14.a and b respectively along four different locations for $x^* = 0$ (○), −0.25 (□), −0.5 (◇) and −0.75 (+). Away from the side channel inlet the horizontal velocity component profiles in the dispersed phase (solid lines) are almost zero (Fig. 14a). When they reach location $y^* = 0.2$, the velocities increase slightly but then significantly decrease towards the interface. The horizontal velocity components in the continuous phase (dashed lines) seem to follow a classical Couette flow profile. The continuous phase velocity magnitude can be seen to increase when the dispersed aqueous phase thickness in the main channel decreases. The vertical velocity profiles are shown in Fig. 14b. As expected, the velocities away from the main channel inlet tend to a plateau corresponding to the

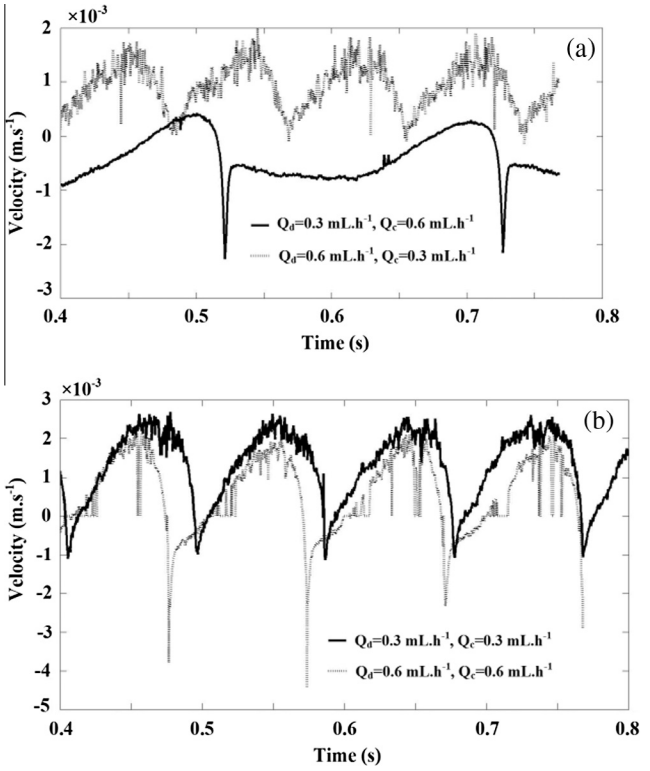

Fig. 11. Horizontal velocity component u versus time. Flowrate combinations (a) Q_d = 0.3 mL h^{-1} and Q_c = 0.6 mL h^{-1} (solid line) and Q_d = 0.6 mL h^{-1} and Q_c = 0.3 - mL h^{-1} (dashed line). (b) Q_d = 0.3 mL h^{-1} and Q_c = 0.3 mL h^{-1} (solid line) and Q_d = 0.6 mL h^{-1} and Q_c = 0.6 mL h^{-1} (dashed line).

aqueous phase flow rate. The maximum absolute vertical velocity is obtained for the position $x_* = -0.5$ (middle of the channel). It is interesting to note the different sign of the velocity in the dispersed and the continuous phase. The continuous phase appears to oppose the dispersed phase entering the main channel.

5. Conclusions

Two different micro Particle Image Velocimetry (μPIV) techniques have been developed for temporally and spatially resolved velocity fields in the two phases during liquid–liquid plug flow formation in a microchannel T-junction. To the authors knowledge this is the first study where velocity fields are recorded during the plug formation process. A water/glycerol solution was used as the aqueous phase and was injected from the side channel of the junction, while silicon oil was the continuous phase. The water to oil flow rate ratios varied from to 0.3 to 3.

The two-colour μPIV technique is characterized by a dual beam laser producing, in the same pulse, two different wavelengths (blue/355 nm, and green/532 nm). These beams illuminate two different particle types, each seeded in one of the phases of the mixture. Red fluorescein coated polystyrene particles were used in the aqueous phase while blue fluorescein coated polystyrene particles were added in the organic phase. The light emitted from the particles was separated in a beam splitter and through a dichroic mirror and filters each wavelength was directed to two separate cameras, one for each phase. This technique has low laser repetition rate but an adjustable time delay between the two laser cavities. Events cannot be followed in time but high velocities can be captured and studied. The two-colour μPIV technique is suitable for produc-

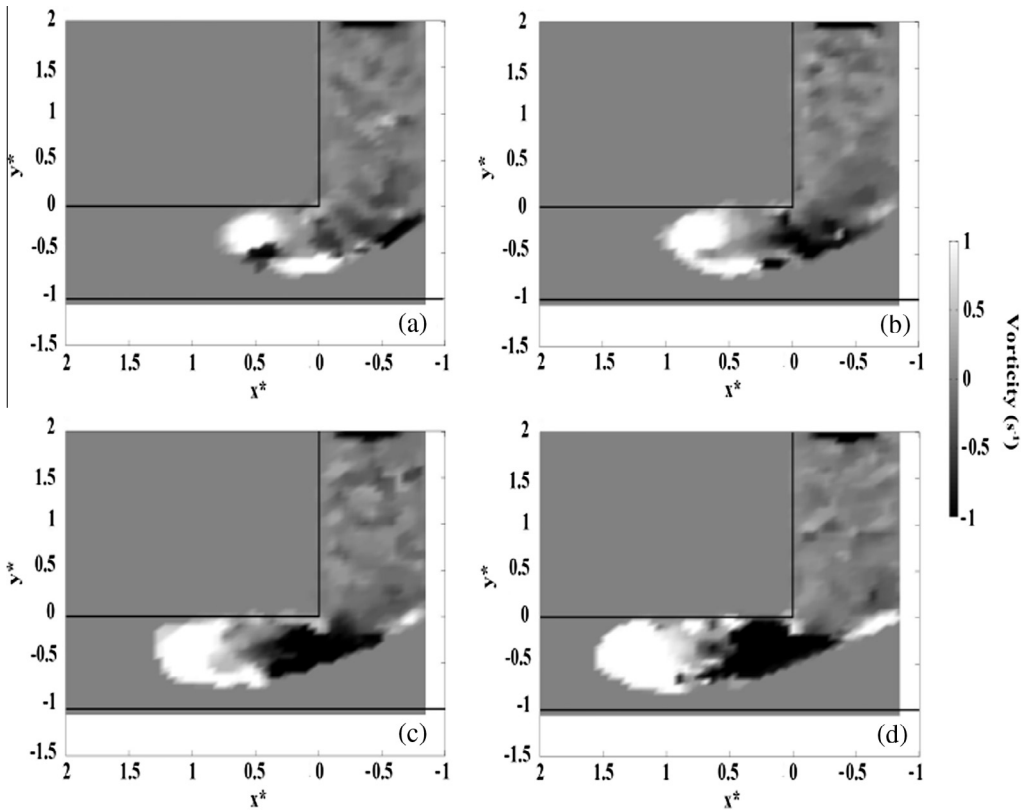

Fig. 12. Vorticity field of the dispersed aqueous phase for flow rate combination Q_c = 0.6 mL h^{-1} and Q_d = 0.3 mL h^{-1} and position of the plug tip (a) 0.75, (b) 1, (c) 1.25 and (d) 1.5. For clarity the boundaries of the channel have been added.

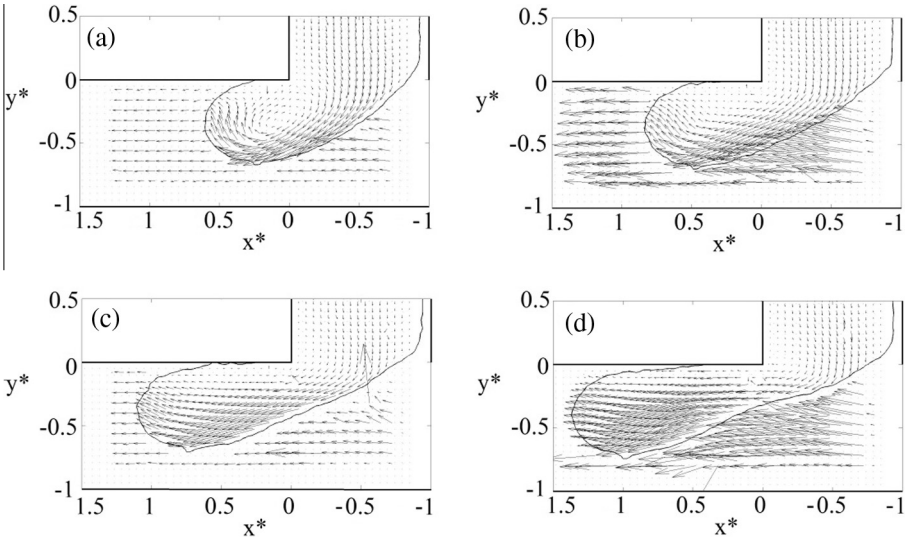

Fig. 13. Velocity fields in both phases for flow rate combination Q_c = 0.6 mL h^{-1} and Q_d = 0.3 mL h^{-1} and position of plug tip (a) 0.5, (b) 0.75, (c) 1 and (d) 1.25. For clarity the boundaries of the channel and the averaged interface position have been added.

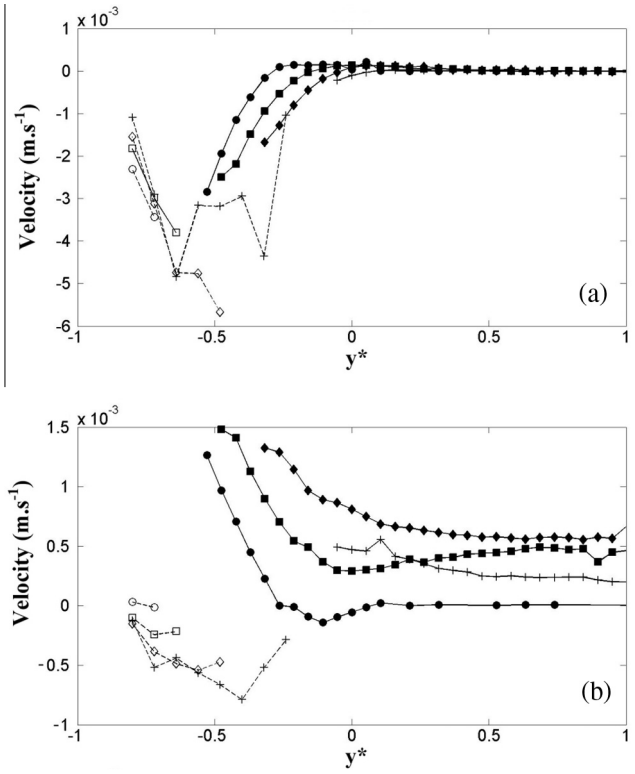

Fig. 14. Horizontal (a) and vertical (b) velocity profiles in both phases for flow rate combination Q_c = 0.6 mL h^{-1} and Q_d = 0.3 mL h^{-1}. The continuous phase is represented by the dashed line while the dispersed phase by the solid line. Velocity profiles are plotted along four different axes located at x^* = 0 (○), −0.25 (□), −0.5 (◇) and −0.75 (+).

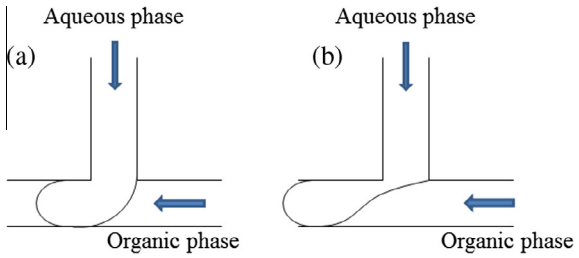

Fig. 15. Schematic showing the interface curvature change at the rear of the plug.

ing phase averaged spatially resolved velocity profiles with high accuracy.

To compute time resolved velocity fields, a high speed bright field μPIV has also been developed. In this technique, the flow channel is illuminated with a white light from the back and the shadows of the tracers seeded in a given phase are recorded by BW contrast imaging over successive frames. Phenomena can be followed in time at the 3 kHz repetition rate of the camera. However, the time delay between successive images is quite large (much larger than in the two colour PIV) and large velocity magnitudes cannot be captured.

The time evolution of the forming plug and the corresponding velocity profiles in the dispersed phase, obtained from the high speed bright field PIV, reveal changes in the hydrodynamic patterns corresponding to different water-to-oil flow rate ratios. In particular, for flow rate ratio equal to one, a large vortex is formed at the tip in the early stage of the plug formation process. It was also found that the interface curvature at the rear of the plug increases until it changes sign (Fig. 15). This change in curvature accelerates the drainage of the meniscus which connects the forming plug with the feeding side channel and leads to meniscus breakage and plug detachment. The phase averaged velocity fields obtained in both phases with the two-colour PIV show that the continuous phase resists the flow into the main channel of the dispersed phase at the rear of the plug meniscus (velocities in the two phases in the vertical direction have opposite signs) and causes the change in the interface curvature.

Acknowledgements

This project was funded under the UK Engineering and Physical Sciences Research Council (EPSRC) Programme Grant MEMPHIS. The authors would like to acknowledge the EPSRC Instrument Pool for the loan of the high-speed camera.

References

[1] R.J. Adrian, Twenty years of particle image velocimetry, Exp. Fluids 39 (2005) 159–169, http://dx.doi.org/10.1007/s00348-005-0991-7.

[2] R.J. Adrian, J. Westerweel, Particle Image Velocimetry, Cambridge University Press, New York, 2011.

[3] P. Angeli, A. Gavriilidis, A hydrodynamics of Taylor flow in small channels: a review, J. Mech. Eng. Sci. 222 (2008) 737–751, http://dx.doi.org/10.1243/09544062JMES776.

[4] D.P. Chakrabarti, G. Das, S. Ray, Pressure drop in liquid–liquid two phase horizontal flow: experiment and prediction, Chem. Eng. Technol. 28 (2005) 1003–1009, http://dx.doi.org/10.1002/ceat.200500143.

[5] R. Daw, J. Finkelstein, Insight: lab on a chip, Nature 442 (7101) (2006) 367–418.

[6] A.L. Dessimoz, L. Cavin, A. Renken, L. Kiwi-Minsker, Liquid–liquid two-phase flow patterns and mass transfer characteristics in rectangular glass microreactors, Chem. Eng. Sci. 63 (16) (2008) 4035–4044, http://dx.doi.org/10.1016/j.ces.2008.05.005.

[7] V. Dore, D. Tsaoulidis, P. Angeli, Mixing patterns in water plugs during water/ionic liquid segmented flow in microchannels, Chem. Eng. Sci. 80 (2012) 334–341, http://dx.doi.org/10.1016/j.ces.2012.06.030.

[8] W.F. Fang, S.C. Ting, C.W. Hsu, Y.T. Chen, J.T. Yang, Locally enhanced concentration and detection of oligonucleotides in a plug-based microfluidic device, Lab. A Chip 12 (5) (2012) 923–931, http://dx.doi.org/10.1039/C2LC20917A.

[9] P. Garstecki, M.J. Fuerstman, H.A. Stone, G.M. Whitesides, Formation of droplets and bubbles in a microfluidic T-junction—scaling and mechanism of break-up, Lab. A Chip 6 (3) (2006) 437–446, http://dx.doi.org/10.1039/B510841A.

[10] A. Ghaini, M.N. Kashid, D.W. Agar, Effective interfacial area for mass transfer in the liquid–liquid slug flow capillary microreactors, Chem. Eng. Process.: Process Intens. 49 (4) (2010) 358–366, http://dx.doi.org/10.1016/j.cep.2010.03.009.

[11] S.M. Hagsäter, C.H. Westergaard, H. Bruus, J.P. Kutter, Investigations on LED illumination for micro-PIV including a novel front-lit configuration, Exp. Fluids 44 (2) (2008) 211–219, http://dx.doi.org/10.1007/s00348-007-0394-z.

[12] J. Husny, J.J. Cooper-White, The effect of elasticity on drop creation in T-shaped microchannels, J. Non-newtonian Fluid Mech. 137 (1) (2006) 121–136, http://dx.doi.org/10.1016/j.jnnfm.2006.03.007.

[13] J. Jovanović, W. Zhou, E.V. Rebrov, T.A. Nijhuis, V. Hessel, J.C. Schouten, Liquid–liquid slug flow: hydrodynamics and pressure drop, Chemical Engineering Science 66 (1) (2011) 42–54, http://dx.doi.org/10.1016/j.ces.2010.09.040.

[14] P. Joseph, P. Tabeling, Direct measurement of the apparent slip length, Physical Review E 71 (3) (2005) 035303, http://dx.doi.org/10.1103/PhysRevE.71.035303.

[15] M.N. Kashid, I. Gerlach, S. Goetz, J. Franzke, J.F. Acker, F. Platte, D.W. Agar, S. Turek, Internal circulation within the liquid slugs of a liquid-liquid slug-flow capillary microreactor, Industrial & engineering chemistry research 44 (14) (2005) 5003–5010, http://dx.doi.org/10.1021/ie0490536.

[16] M.N. Kashid, D.W. Agar, Hydrodynamics of liquid–liquid slug flow capillary microreactor: flow regimes, slug size and pressure drop, Chemical Engineering Journal 131 (1) (2007) 1–13, http://dx.doi.org/10.1016/j.cej.2006.11.020.

[17] M.N. Kashid, F. Platte, D.W. Agar, S. Turek, Computational modelling of slug flow in a capillary microreactor, Journal of Computational and Applied Mathematics 203 (2) (2007) 487–497, http://dx.doi.org/10.1016/j.cam.2006.04.010.

[18] M.N. Kashid, D.F. Rivas, D.W. Agar, S. Turek, On the hydrodynamics of liquid–liquid slug flow capillary microreactors, Asia-Pacific Journal of Chemical Engineering 3 (2) (2008) 151–160, http://dx.doi.org/10.1002/apj.127.

[19] M.N. Kashid, A. Renken, L. Kiwi-Minsker, CFD modelling of liquid–liquid multiphase microstructured reactor: Slug flow generation, Chemical Engineering Research and Design 88 (3) (2010) 362–368, http://dx.doi.org/10.1016/j.cherd.2009.11.017.

[20] M. Kashid, L. Kiwi-Minsker, Quantitative prediction of flow patterns in liquid–liquid flow in micro-capillaries, Chemical Engineering and Processing: Process Intensification 50 (10) (2011) 972–978, http://dx.doi.org/10.1016/j.cep.2011.07.003.

[21] H. Kinoshita, S. Kaneda, T. Fujii, M. Oshima, Three-dimensional measurement and visualization of internal flow of a moving droplet using confocal micro-PIV, Lab on a Chip 7 (3) (2007) 338–346, http://dx.doi.org/10.1039/B617391H.

[22] X.B. Li, F.C. Li, J.C. Yang, H. Kinoshita, M. Oishi, M. Oshima, Study on the mechanism of droplet formation in T-junction microchannel, Chem. Eng. Sci. 69 (1) (2012) 340–351, http://dx.doi.org/10.1016/j.ces.2011.10.048.

[23] C.D. Meinhart, S.T. Wereley, J.G. Santiago, PIV measurements of a microchannel flow, Exp. Fluids 27 (5) (1999) 414–419, http://dx.doi.org/10.1007/s003480050366.

[24] Z. Mohamed-Kassim, E.K. Longmire, Drop coalescence through a liquid/liquid interface, Phys. Fluids 16 (7) (2004) 2170–2181, http://dx.doi.org/10.1063/1.1735686.

[25] T. Nisisako, T. Torii, T. Higuchi, Novel microreactors for functional polymer beads, Chem. Eng. J. 101 (1) (2004) 23–29, http://dx.doi.org/10.1016/j.cej.2003.11.019.

[26] H. Nobach, E. Bodenschatz, Limitations of accuracy in PIV due to individual variations of particle image intensities, Exp. Fluids 47 (1) (2009) 27–38, http://dx.doi.org/10.1007/s00348-009-0627-4.

[27] M. Oishi, H. Kinoshita, T. Fujii, M. Oshima, Confocal micro-PIV measurement of droplet formation in a T-shaped micro-junction, J. Phys.: Conf. Ser. 147 (1) (2009) 012061, http://dx.doi.org/10.1088/1742-6596/147/1/012061.

[28] M. Oishi, H. Kinoshita, T. Fujii, M. Oshima, Simultaneous measurement of internal and surrounding flows of a moving droplet using multicolour confocal micro-particle image velocimetry (micro-PIV), Meas. Sci. Technol. 22 (10) (2011) 105401, http://dx.doi.org/10.1088/0957-0233/22/10/105401.

[29] M. Raffel, C.E. Willert, J. Kompenhans, Particle Image Velocimetry: A Practical Guide, Springer, 1998.

[30] R. Raj, N. Mathur, V.V. Buwa, Numerical simulations of liquid– liquid flows in microchannels, Ind. Eng. Chem. Res. 49 (210) (2010) 10606–10614, http://dx.doi.org/10.1021/ie100626a.

[31] M. Rossi, R. Segura, C. Cierpka, C.J. Kähler, On the effect of particle image intensity and image preprocessing on the depth of correlation in micro-PIV, Exp. Fluids 52 (4) (2012) 1063–1075, http://dx.doi.org/10.1007/s00348-011-1194-z.

[32] A. Salim, M. Fourar, J. Pironon, J. Sausse, Oil–water two phase flow in microchannels: flow patterns and pressure drop measurements, Can. J. Chem. Eng. 86 (6) (2008) 978–988, http://dx.doi.org/10.1002/cjce.20108.

[33] J.G. Santiago, S.T. Wereley, C.D. Meinhart, D.J. Beebe, R.J. Adrian, A particle image velocimetry system for microfluidics, Exp. Fluids 25 (4) (1998) 316–319, http://dx.doi.org/10.1007/s003480050235.

[34] F. Sarrazin, K. Loubiere, L. Prat, C. Gourdon, T. Bonometti, J. Magnaudet, Experimental and numerical study of droplets hydrodynamics in microchannels, AIChE J. 52 (12) (2006) 4061–4070, http://dx.doi.org/10.1002/aic.11033.

[35] M. Stanislas, K. Okamoto, C.J. Kähler, J. Westerweel, F. Scarano, Main results of the third international PIV challenge, Exp. Fluids 45 (1) (2008) 27–71, http://dx.doi.org/10.1007/s00348-008-0462-z.

[36] S.W. Stone, C.D. Meinhart, S.T. Wereley, A microfluidic-based nanoscope, Exp. Fluids 33 (5) (2002) 613–619, http://dx.doi.org/10.1007/s00348-001-0379-2.

[37] R. Theunissen, F. Scarano, M.L. Riethmuller, On improvement of PIV image interrogation near stationary interfaces, Exp. Fluids 45 (4) (2008) 557–572, http://dx.doi.org/10.1007/s00348-008-0481-9.

[38] D. Tsaoulidis, V. Dore, P. Angeli, N.V. Plechkova, K.R. Seddon, Flow patterns and pressure drop of ionic liquid–water two-phase flows in microchannels, Int. J. Multiphase Flow 54 (2013) 1–10, http://dx.doi.org/10.1016/j.ijmultiphaseflow.2013.02.002.

[39] D. Tsaoulidis, Studies of intensified small-scale processes for liquid-liquid separations in spent nuclear fuel reprocessing. Doctoral dissertation, University College London, 2014.

[40] J. Westerweel, Fundamentals of digital particle image velocimetry, Meas. Sci. Technol. 8 (1997) 1379–1392.

[41] E. Yamaguchi, B.J. Smith, D.P. Gaver, μ-PIV measurements of the ensemble flow fields surrounding a migrating semi-infinite bubble, Exp. Fluids 47 (2) (2009) 309–320, http://dx.doi.org/10.1007/s00348-009-0662-1.

[42] Y. Zhao, G. Chen, Q. Yuan, Liquid-liquid two-phase flow patterns in a rectangular microchannel, AIChE J. 52 (12) (2006) 4052–4060, http://dx.doi.org/10.1002/aic.11029.